

Automated Digital Microfluidic Platform for Magnetic-Particle-Based Immunoassays with Optimization by Design of Experiments

Kihwan Choi,^{†,§,∇} Alphonsus H. C. Ng,^{‡,§,∇} Ryan Fobel,^{‡,§} David A. Chang-Yen,^{||} Lyle E. Yarnell,[⊥] Elroy L. Pearson,^{||} Carl M. Oleksak,[⊥] Andrew T. Fischer,[⊥] Robert P. Luoma,[⊥] John M. Robinson,[#] Julie Audet,^{‡,§} and Aaron R. Wheeler^{*,†,‡,§}

[†]Department of Chemistry, University of Toronto, 80 St. George Street, Toronto, Ontario M5S 3H6, Canada

[‡]Institute of Biomaterials and Biomedical Engineering, University of Toronto, 164 College Street, Toronto, Ontario M5S 3G9, Canada

[§]Donnelly Centre for Cellular and Biomolecular Research, 160 College Street, Toronto, Ontario M5S 3E1, Canada

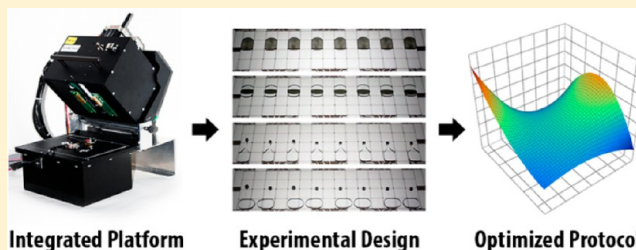
^{||}AbbVie, 200 Abbott Park Road, Abbott Park, Illinois 60064, United States

[⊥]Abbott Diagnostics, 1921 Hurd Drive, Irving, Texas 75038, United States

[#]Abbott Diagnostics, 100 Abbott Park Road, Abbott Park, Illinois 60064, United States

S Supporting Information

ABSTRACT: We introduce an automated digital microfluidic (DMF) platform capable of performing immunoassays from sample to analysis with minimal manual intervention. This platform features (a) a 90 Pogo pin interface for digital microfluidic control, (b) an integrated (and motorized) photomultiplier tube for chemiluminescent detection, and (c) a magnetic lens assembly which focuses magnetic fields into a narrow region on the surface of the DMF device, facilitating up to eight simultaneous digital microfluidic magnetic separations. The new platform was used to implement a three-level full factorial design of experiments (DOE) optimization for thyroid-stimulating hormone immunoassays, varying (1) the analyte concentration, (2) the sample incubation time, and (3) the sample volume, resulting in an optimized protocol that reduced the detection limit and sample incubation time by up to 5-fold and 2-fold, respectively, relative to those from previous work. To our knowledge, this is the first report of a DOE optimization for immunoassays in a microfluidic system of any format. We propose that this new platform paves the way for a benchtop tool that is useful for implementing immunoassays in near-patient settings, including community hospitals, physicians' offices, and small clinical laboratories.



The *in vitro* diagnostic industry is dominated by robotic immunoanalyzers—the gold standard for high-throughput protein and small-molecule quantitation.¹ These instruments are capable of quantifying disease biomarkers from patient samples at clinically relevant concentrations at a rate of hundreds of tests per hour. Importantly, the throughput of these instruments allows developers to rapidly determine optimal assay parameters via a design of experiments (DOE) approach,^{2,3} leading to reduced assay development and optimization timelines.⁴ Unfortunately, robotic immunoanalyzers are large, complex instruments found only in well-funded centralized facilities such as hospital reference laboratories, to which patient samples are transported after collection. As healthcare costs continue to rise, the global *in vitro* diagnostic market is gradually shifting from centralized facilities to point of care testing (POCT).⁵ This market trend is facilitated by technological advances in nanomaterials,⁶ integrated sensors,⁷ and microfluidics.⁸ In particular, microfluidics is proving useful for the miniaturization of liquid handling, leading to the development of various microfluidic immunoassay systems⁹ and

the commercialization of these platforms.¹⁰ To date, however, there have been no reports of DOE optimization of microfluidic immunoassays, likely because of a lack of automation, parallelization, and control.

While most miniaturized immunoassay systems rely on enclosed microchannels,^{11–13} several groups are exploring the use of an alternative open surface format, known as digital microfluidics (DMF).^{14–16} In DMF, fluids are electrostatically manipulated in discrete droplets (picoliter to microliter sized) on an open array of electrodes coated with a hydrophobic insulator. When appropriate sequences of potentials are applied to these electrodes, the droplets can be driven to mix, merge, split, and be metered from reservoirs.¹⁷ Droplet movement sequences can be reprogrammed to accommodate different experimental conditions (e.g., incubation time and volume)

Received: June 19, 2013

Accepted: August 2, 2013

Published: August 26, 2013

without the need for a new device design. The most established approach to DMF immunoassays uses magnetic particles for antibody solid support and relies on oil carrier fluid to enable aqueous droplet movement.¹⁸ Using this method, immunoassays for insulin,¹⁸ interleukin-6,¹⁸ troponin I,¹⁹ immunoglobulin E,²⁰ and the hypercoagulability panel²¹ have been implemented in benchtop digital microfluidic instruments with integrated fluorescent detection. These demonstrations, though few, represent important milestones toward DMF-powered near-patient analysis, or even (eventually) POCT.

A new approach to DMF immunoassays eliminates the need for oil carrier fluid and improves the washing efficiency of magnetic particles using a technique called digital microfluidic magnetic separation. The first report²² describing this method demonstrated utility for quantifying 17 β -estradiol and thyroid-stimulating hormone (TSH) at clinically relevant levels, with 100-fold and 10-fold reductions in reagent volumes and analysis times relative to those of conventional systems, but this initial demonstration was carried out using a prototype setup, requiring significant manual involvement for assay implementation. Specifically, droplet sequences were delivered using hand-held voltage probes, the magnet position was manually adjusted for particle separation, and measurement of the chemiluminescent signal was performed off-line in a commercial well-plate reader.

Here, we report a significant improvement over the initial method,²² centered on the development and characterization of an automated platform capable of performing complete immunoassays with minimal manual intervention. This platform features a 90 Pogo pin interface for digital microfluidic control, an integrated (and motorized) photomultiplier tube (PMT) for chemiluminescent detection, and a new magnet assembly for particle separation. The latter, called a "magnetic lens", focuses magnetic fields into a narrow region on the surface of the DMF device, facilitating up to eight simultaneous digital microfluidic magnetic separations. This new platform was used to implement a three-level full factorial DOE optimization of immunoassays, varying (1) the analyte concentration, (2) the sample incubation time, and (3) the sample volume. The resulting optimized protocol reduced the detection limit and sample incubation time by up to 5-fold and 2-fold, respectively, relative to those from previous work.²² More importantly, these results establish digital microfluidics as a useful tool for implementing DOE optimization; to our knowledge, this is the first report of DOE optimization for immunoassays in any type of microfluidic system. We propose that the new platform has great potential for the quantitative analysis of disease biomarkers in various near-patient settings, including community hospitals, physicians' offices, and small clinical laboratories.

■ EXPERIMENTAL SECTION

Reagents and Materials. Unless otherwise specified, reagents were purchased from Sigma Chemical (Oakville, ON). Deionized water had a resistivity of 18 M Ω ·cm at 25 °C. Pluronic L64 (BASF Corp., Germany) was generously donated by Brenntag Canada (Toronto, ON).

On-Chip Immunoassay Reagents. Reagent solutions used on-chip were either obtained from vendors or custom-made in-house. Reagents from vendors include TSH standards and antibody-coated paramagnetic microparticles from Abbott Laboratories (Abbott Park, IL), horseradish peroxidase (HRP)-conjugated mouse monoclonal anti-TSH from Abcam Inc.

(Cambridge, MA), and SuperSignal ELISA Femto chemiluminescent substrate, comprising stable peroxide (H₂O₂) and luminol-enhancer solution, from Thermo Fischer Scientific (Rockford, IL). Custom DMF-compatible wash buffer and conjugate diluent were prepared as described previously.²² DMF-compatible particle diluent (pH 10) was formed from Tris base (6.1 g/L), NaCl (5.8 g/L), bovine serum albumin (BSA) (1%, w/v), thimerosal (0.05%, w/v), and L64 (0.05%, v/v). Prior to use, the TSH standards and chemiluminescent substrate were supplemented with Pluronic L64 at 0.05% and 0.025%, v/v, respectively. TSH conjugate working solutions were formed by diluting HRP-conjugated anti-TSH (2 μ g/mL) in conjugate diluent. The microparticle working solution was formed by resuspending microparticles in particle diluent at $\sim 3.0 \times 10^8$ particles/mL.

Device Fabrication and Operation. Digital microfluidic devices, each comprising a bottom plate and top plate, were fabricated in the University of Toronto Nanofabrication Centre (TNFC) cleanroom facility and were assembled as described previously.²² The bottom-plate device design featured an array of 80 actuation electrodes (2.2 \times 2.2 mm each) connected to 8 reservoir electrodes (16.4 \times 6.7 mm each) and 4 waste reservoir electrodes (16.4 \times 6.4 mm each). The actuation electrodes were roughly square with interdigitated borders (140 μ m peak to peak sinusoids) and interelectrode gaps of 30–80 μ m. Unit droplet and reservoir droplet volumes on these devices were ~ 800 nL and ~ 3.5 μ L, respectively.

An automated platform (Figure 1) was designed and built to manage droplet operation, the magnet and PMT position, and data collection. Droplet movement was controlled via the open-source Microdrop software and an Arduino-based (Smart Projects, Italy) high-voltage switching instrument described in detail elsewhere.²³ A custom plug-in for the Microdrop software was used to control the motors in the platform, read signals from their respective optical limit switches, and trigger PMT reading. Signals from the PMT were processed using a CT2 counter timer module (ET Enterprises, Sweetwater, TX) connected to a computer via an RS232 interface and recorded (at a period of 1 s) using the associated EM6 counter timer software. An integrated light-emitting diode (LED) and webcam assembly was used to monitor on-chip droplet movement prior to analysis. All hardware components fit in a benchtop form factor enclosure (approximate dimensions 18 \times 23 \times 30 cm).

To load a DMF device onto the platform, the hinge-based enclosure is opened, and the DMF device is positioned on the device holder, connecting the top plate with the grounded brass leaflets (Figure S1 in the Supporting Information). When the device is secured in the holder, the enclosure is closed, and the Pogo pins are lowered onto the device (via a motor and two optical limit switches) to form a secure electrical connection with the exposed contact pads on the bottom plate. The electrical interface comprises a pair of 15 \times 3 Pogo pin arrays with center-to-center spacing of 100 mil, capable of delivering 90 individual voltage inputs (Figure 1A). To drive droplet movement, a sine wave ac potential (100–120 V_{RMS}, 10 kHz) was applied between the top plate (ground) and sequential electrodes on the bottom plate. Reagent reservoirs were filled by pipetting the reagent adjacent to the gap between the bottom and top plates and applying a driving potential to a reservoir electrode. Waste and unused reservoir fluids were removed with KimWipes (Kimberly-Clark, Irving, TX). Unit droplets were dispensed from the reservoirs, moved, merged,

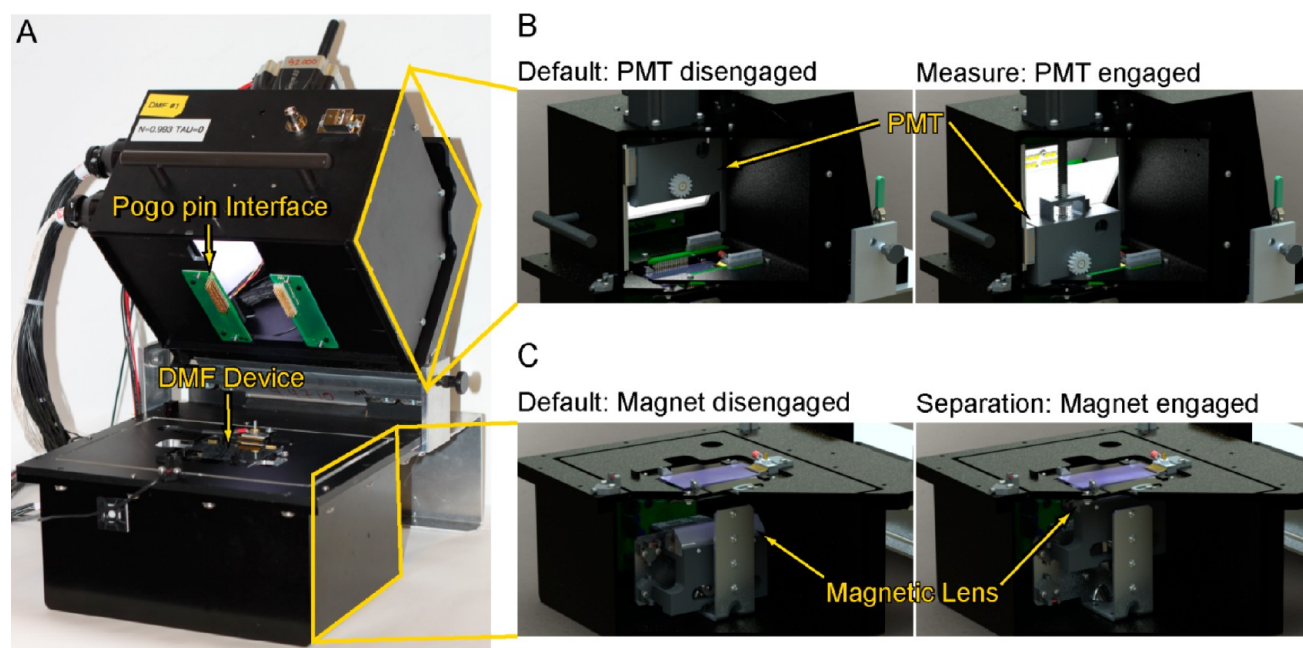


Figure 1. Integrated platform for digital microfluidic particle-based immunoassays. (A) Photograph of the automation setup (opened orientation) with labels showing the DMF device and Pogo pin interface. (B) Cross-sectional computer-aided design (CAD) rendering of the integrated PMT in the default (left) or measure (right) state. (C) Cross-sectional CAD rendering of the motor-controlled magnet in the default (left) or separation (right) state. The automation setup is in closed orientation in (B) and (C).

and mixed as described previously.¹⁷ To perform a mixing operation, a unit droplet was shuttled in a circular motion across four electrodes; more electrodes were used for larger droplets.

Measurements with an Integrated PMT. The automated control system includes an integrated Hamamatsu H10682-110 PMT with a 5 V dc source. The bias voltage and discrimination level for the PMT were preset by the manufacturer to optimal values. Using a motor and two optical limit switches, the vertical position of the PMT can be adjusted to either the disengaged state (default) or the engaged state (Figure 1B). In the disengaged state, the PMT is positioned ~ 5 cm above the DMF device and the sensor orifice is protected from ambient light by a shutter. In the engaged state, the shutter is opened and the PMT is positioned several hundred micrometers above the DMF device, allowing the collection of light emitted from the surface of the device.

Magnetic Lens and Modeling. The automated control system includes a motor-driven magnet assembly positioned beneath the center of the device (Figure 1C and Figure S1 in the Supporting Information). The magnet assembly, called a “magnetic lens”, comprises a neodymium magnet bar (3 in. \times 1/2 in. \times 1/4 in. thick, relative permeability $\mu_r = 1.05$, remnant field strength $B_r = 1.32$ T) flanked by two steel (AISI 1080) machined armatures (Figure 2A). Using a motor and two optical limit switches, the vertical position of the magnet can be adjusted to either the disengaged state (default) or the engaged state (for particle separation). In the disengaged state, the magnet is positioned ~ 3.8 cm below the device. In the engaged state, the magnet is positioned ~ 150 μm below the device.

Magnetic forces exerted on particles by the new magnetic lens (described above) and the magnet system used previously²² (i.e., a 5/8 in. diameter \times 1/4 in. thick neodymium disc with relative permeability $\mu_r = 1.05$ and remnant field strength $B_r = 1.38$ T) were modeled using finite element analysis software (COMSOL, Burlington, MA; 3D model with

magnetic fields and no currents). Magnetic particles are assumed to have diameters of 5 μm and magnetic susceptibility $\chi = 1.05$,²⁴ and a pellet of particles is represented geometrically as a sphere with volume equal to the volume of one particle multiplied by the number of particles. For example, for a particle density of 3.0×10^8 particles/mL and a droplet volume of 800 nL, the pellet has a radius of 155 μm . The distance between the particle pellet and the magnet was assumed to be 1.4 mm, which takes into account the thickness of the bottom plate (~ 1.15 mm) and the tolerance of the setup. The magnetic force on the pellet (both the y -component and x -component) was calculated as a function of the horizontal and vertical pellet positions.²⁵

Pilot Immunoassays and DOE Analysis. Using DMF magnetic separation for reagent exchange and particle washing as described previously,²² pilot on-chip immunoassays for DOE analysis were implemented in seven steps: (1) A droplet containing paramagnetic particles was dispensed from a reservoir and separated from the diluent. (2) One, three, or five droplets (representing 0.8, 2.4, or 4 μL after merging) of TSH standards (0, 0.4, or 4 $\mu\text{IU/mL}$) were dispensed, delivered to the immobilized particles, and mixed for 3, 6, or 9 min. (3) The particles were washed four times in wash buffer and separated from the supernatant. (4) One droplet of HRP conjugate solution was dispensed, delivered to the immobilized particles, and mixed for 2 min. (5) The particles were washed five times in wash buffer; after the fifth wash, the particles were kept suspended in wash buffer and queued for analysis. (6) The particles were separated from the wash buffer and resuspended in one droplet of H_2O_2 , and this droplet was merged and mixed (for 40 s) with one droplet of luminol-enhancer solution. (7) The pooled droplet was incubated for 100 s, and the chemiluminescent signal was recorded using the integrated PMT. In these assays, two experiments were run simultaneously and four replicates were evaluated for each condition. The ratio of the chemiluminescent signal from each sample relative to the

average signal generated from the blank ($0 \mu\text{IU/mL}$ TSH) was collected for each sample volume and sample incubation time. These measured signal-to-background ratio (SBR) responses were fitted via centered polynomial regression²⁶ using a modified second-order model:

$$\begin{aligned}\hat{Y} = & I + \beta_1 X_1 + \beta_2 X_2 + \beta_3 X_3 + \beta_{12} X_1 X_2 + \beta_{13} X_1 X_3 \\ & + \beta_{23} X_2 X_3 + \beta_{11} X_1^2 + \beta_{22} X_2^2 + \beta_{33} X_3^2 + \beta_{122} X_1 X_2^2 \\ & + \beta_{133} X_1 X_3^2 + \beta_{211} X_2 X_1^2 + \beta_{233} X_2 X_3^2 + \beta_{311} X_3 X_1^2 \\ & + \beta_{322} X_3 X_2^2\end{aligned}\quad (1)$$

where \hat{Y} is the predicted response, I is the constant term, β_i is the coefficient (effect) of factor X_i , β_{ij} is the coefficient of the two-factor interaction $X_i X_j$, β_{ii} is the coefficient of the quadratic factor X_i^2 , and β_{ijj} is the coefficient of the linear \times quadratic interaction factor $X_i X_j^2$. Statistical analysis, model construction, and data interpretation were performed using the JMP 10 statistical analysis package (SAS Institute Inc., Cary, NC).

Optimized Immunoassays. The optimized immunoassay method was similar to that of the pilot protocol, with three changes. First, in step 1, optimized assays used five droplets of TSH standards (0 , 0.4 , or $4 \mu\text{IU/mL}$) and the particles were mixed for 3 min. Second, in steps 5 and 6, the particles were washed four times in wash buffer and separated from the supernatant and chemiluminescent reaction was initiated immediately. Finally, in step 7, the chemiluminescent substrate and particles were mixed for 4 min and the signal was collected after 10 s using the integrated PMT. Four measurements at each concentration were averaged and fitted to a linear equation. The limit of detection (LOD) for this assay was the concentration corresponding to the position on the curve of the average signal generated from blank measurements plus 3 times the standard deviation of the blank measurements.

RESULTS AND DISCUSSION

Automated Immunoassay Platform. We designed and built an integrated platform capable of performing immunoassays with minimal manual intervention (Figure 1A). The platform comprises three core components: a Pogo pin interface for digital microfluidic control, an integrated PMT for chemiluminescent detection, and an adjustable magnet for particle separation. These components fit in a light-tight, shoebox-sized enclosure; in the absence of a chemiluminescent reaction, the photon count rate inside the enclosure was less than 50 counts/s, within the specifications of a typical dark count rate for this PMT.

The use of Pogo pins as an electronic interface to control droplet movement provided several improvements over previous approaches.^{22,27} First, the new interface allowed us to distribute 90 individual high-voltage inputs on a 3×2 in. DMF device (i.e., 15 inputs per square inch), allowing for much higher density than for configurations reported previously (4–7 inputs per square inch^{19,28}). Second, compared to slot connectors,²⁷ device loading using Pogo pins is more straightforward; after a device is placed in the device holder, the Pogo pins are lowered (via a motor) to automatically form secure electrical contacts. Third, the Pogo pin interface is compatible with a wide range of substrate material and thickness. Although the current project uses bottom-plate substrates with ~ 1.15 mm thickness, this same interface is compatible with thinner or thicker substrates (data not shown).

We evaluated the performance of the integrated PMT by employing digital microfluidic homogeneous enzyme assays²⁹ using HRP and luminol– H_2O_2 -based chemiluminescent substrate. In these assays, HRP standards and substrate solution were dispensed and mixed using digital microfluidics, generating a chemiluminescent product with light intensity proportional to the HRP concentration. As a comparison, these assays were also analyzed using a commercial well-plate reader used in previous immunoassay work.²² As shown in Figure S2 in the Supporting Information, the calibration curves measured by both methods were linear and had a dynamic range of at least 2 orders of magnitude. Importantly, the coefficients of variation (CVs) for the measurements generated using the integrated PMT (0.56–9.3%) are lower than those from the well-plate reader (0.63–21%). In addition, the integrated PMT method had a slightly lower LOD compared to that of the well-plate reader (4.88 vs 7.97 $\mu\text{IU/mL}$). We speculate that the improved performance is related to the reproducible positioning of the detector and device (in one package), in contrast to manual insertion of devices into a well-plate reader.

Magnet Design and Modeling. Although digital microfluidic magnetic separation is proving to be a useful and efficient method for the extraction and cleanup of specific analytes, its successful implementation requires an adjustable magnet that can induce sufficient force on particles inside a droplet.²² In previous work,^{22,28} this requirement was satisfied by an off-the-shelf neodymium magnet disc which was introduced or removed from the DMF device during magnetic separation or resuspension, respectively, facilitating up to two simultaneous digital microfluidic magnetic separations. We attempted to improve on the performance of this format by designing a new system that can satisfy several competing requirements: (1) simple to fabricate, assemble, and automate, (2) increased number of parallel assays, (3) narrower area of effect such that magnetic induction is minimal outside the separation zone, and (4) stronger magnetic field gradient inside the separation zone for faster separations and greater flexibility in the distance between the magnet and the device. After several design iterations (data not shown), we finalized a unique magnet assembly design we call the “magnetic lens” comprising a neodymium magnet bar flanked by two steel machined armatures that act as field directors (Figure 2A). This arrangement focuses the magnetic field to the tips of the two triangular steel poles, forming a strong field gradient at the apex of the assembly. When this magnet assembly is positioned under a DMF device along its width (Figure 1C), a separation zone is formed across the middle of the electrode array (Figure S1 in the Supporting Information). The magnetic lens design has several salient advantages over magnet discs used in previous work,²² as described below.

The first advantage of the magnetic lens is the localization of the field to a narrow area, minimizing unintended particle attraction away from the separation zone (e.g., in the magnetic particle reservoir). As shown in the numerical simulations (Figure 2C and Figure S3A in the Supporting Information), the vertical and horizontal components of the force originating from the magnetic lens acting on a particle pellet (located 1.4 mm above the magnet) fall off rapidly as the particle pellet is moved away from the center of the magnet; these forces become negligible ($<35 \mu\text{N}$) at greater than 4 mm from the center. In contrast, the magnetic fields in the system used previously²² (i.e., an unmodified magnet disc) cover a wide region of the device, often causing unintended particle

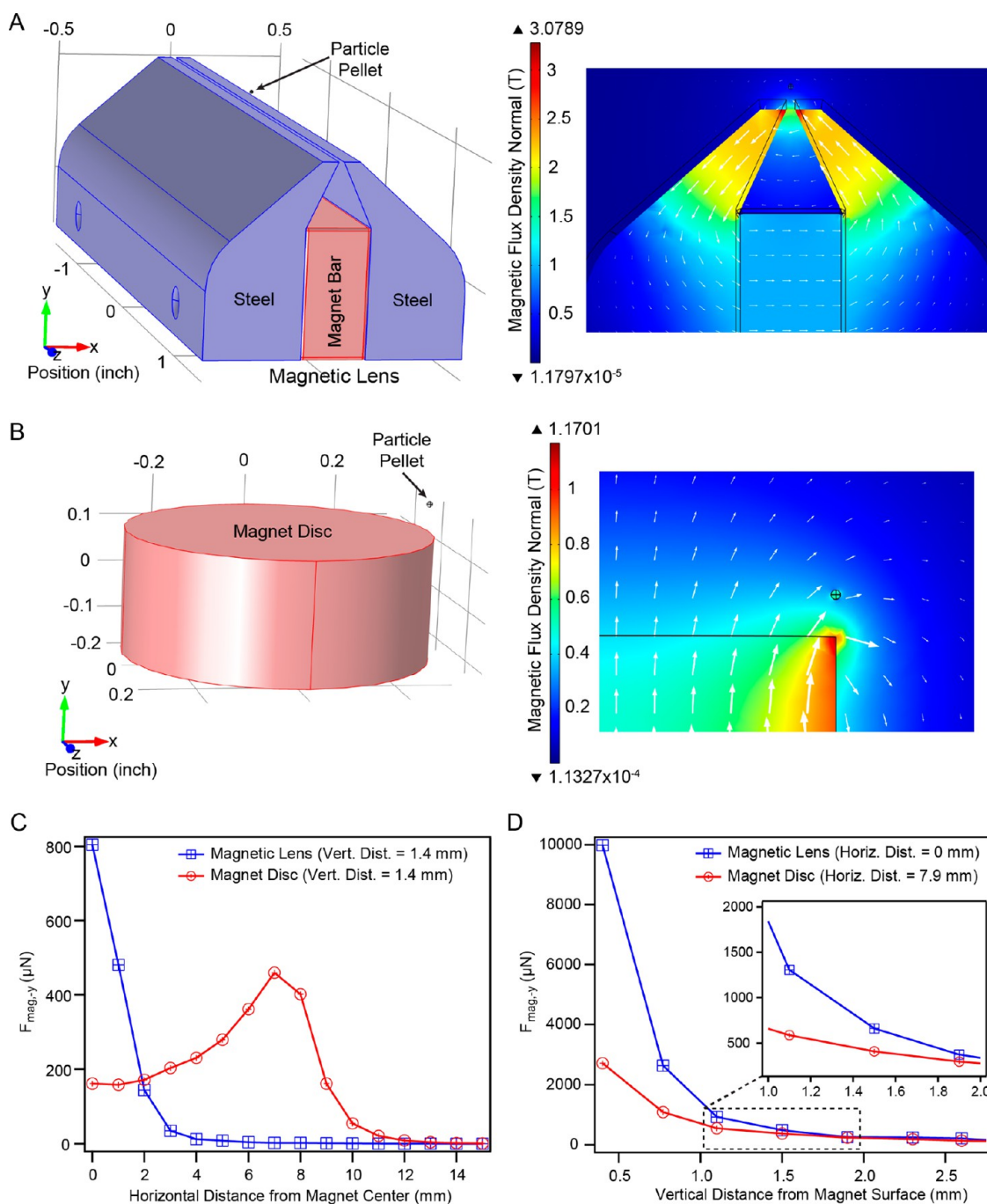


Figure 2. Comparison of forces for the magnetic lens (new design) and the magnet disc (previous approach²²). (A) Schematic of the magnetic lens and numerical modeling of the magnetic flux density normal (heat map with red = high field and blue = low field) and field lines. (B) Schematic of the magnet disc and numerical modeling of the magnetic flux density normal (heat map) and field lines. Force on the particle pellet (directed vertically toward the magnet) as a function of (C) the horizontal position from the magnet center and (D) the vertical position from the magnet surface.

attraction outside the separation zone. For example, according to numerical simulations, a particle pellet positioned 10 mm from the center of a magnetic disc (i.e., not in a position in which trapping is desired) experiences vertical and horizontal forces of ~ 50 and ~ 100 μN , respectively. This phenomenon is exacerbated when the disc is moved horizontally to transition between engaged and disengaged states as in previous work.²² In the new magnet design reported here, this problem is circumvented because the magnet is moved vertically by engaging a motor (Figure 1C).

The second advantage of the magnetic lens is the induction of a stronger magnetic force on the particles in the separation zone relative to that of the magnet disc. In particular, the vertical force increases exponentially as the vertical distance between the particle pellet and magnetic lens decreases (Figure 2D). This distance is limited to the thickness of the device substrate and the separation between the device and the magnet. In previous work, it was determined that a minimum vertical force of ~ 470 μN was required to effectively immobilize the particles for separation,²² which was achievable

only when the magnetic disc made direct contact with the bottom of the device. In contrast, with the magnetic lens system introduced here, magnetic separation is achievable with a $\sim 150\ \mu\text{m}$ gap between the magnet and the device. As in the inset in Figure 2D, this configuration corresponds to a vertical force of $\sim 600\ \mu\text{N}$. From a design standpoint, this gap allowance is desirable for preventing the magnet from colliding with the device.

The third advantage of the magnetic lens system is the facilitation of parallel magnetic separations. As shown in Figure 3, when the magnet is engaged, magnetic particles inside eight droplets pellet on the surface of the device above the magnet. The immobilized particles can then be separated from the supernatant by moving the droplets away, leaving eight pellets of particles on the device surface. Subsequently, the particles can be collected and resuspended by disengaging the magnet,

1) Move Particle Suspension to Separation Zone



2) Engage Magnet



3) Separate Supernatant from Particles



4) Remove Supernatant to Waste



5) Dispense Exchange Solution



6) Disengage Magnet and Reconstitute Particles



7) Resuspend Particles in Solution



Figure 3. Frames from a movie depicting eight parallel particle separation and resuspension cycles on-chip.

moving a droplet of exchange reagent over the particles, and mixing the droplet. In the future, the multiplexing could be increased with a longer magnet or smaller electrode design. In contrast, when using the magnetic disc geometry used previously,²² it is difficult to achieve more than two separations, with no possibility for expansion.

Design of Experiments Analysis for TSH Immunoassays. An immunoassay for TSH was chosen as a test case for the new system, given the wide prevalence of this assay in routine clinical testing for thyroid disease.³⁰ To determine the optimal assay parameters for this new integrated platform, we implemented a 3^3 full factorial DOE for TSH immunoassays. Although there are more efficient methods such as the central composite design,^{31–33} the 3-level full factorial design represents an elaborate test case, suitable for the evaluation of the new automated platform. As a starting point, we varied three factors: sample volume (*vol*; one, three, and five pooled unit droplets), sample incubation time (*inc*; 3, 6, and 9 min), and concentration (*con*, 0, 0.4, and 4 $\mu\text{IU}/\text{mL}$). With replicates, this translated to a total of 108 discrete experiments, a number that would have been very tedious using the nonautomated system described previously.²²

The three-level DOE design allowed us to estimate linear, nonlinear, and interaction effects of all of the tested factors.⁴ The midlevels for *vol* and *inc* were selected to be the same as the optimal parameters in the prototype setup from previous work²² (three unit droplets and 6 min). A pilot immunoassay protocol (described in the Experimental Section) was used in these experiments, in which TSH is quantified using antibody-coated magnetic particles, HRP-conjugated detection antibody, and luminol– H_2O_2 -based chemiluminescent substrate. The signal-to-background ratios (SBRs) from these assays were used as the measured response for DOE optimization.

The results from the full factorial experiment were evaluated in three steps: (1) model construction and validation, (2) identification of significant factors, and (3) prediction of optimal assay parameters. In the first step, the SBR was fitted with a modified second-order model (eq 1), which included linear, quadratic, and interaction factors.^{34,35} However, this initial fit resulted in residual values (i.e., differences between actual and predicted SBRs) that are not distributed normally, suggesting that a response transform was required to meet the fundamental assumptions of standard least-squares multiple regression. A Box-Cox plot confirmed that a power transform of ~ 0.5 minimized the sum of squares error, and therefore, a square-root transform was applied to the SBR. The transformed response, $\text{Sqrt}(\text{SBR})$, was refitted with eq 1, and the fit quality was assessed using several diagnostic tests: (a) according to the Shapiro–Wilk test and normal probability plot, the residual values were normally distributed (Figure 4A), (b) as shown in Figure 4B, the predicted $\text{Sqrt}(\text{SBR})$ was well correlated with the actual $\text{Sqrt}(\text{SBR})$, (c) the R^2 and adjusted R^2 values were 0.90 and 0.88, respectively, and (d) the factors in the model have a significant effect ($p < 0.0001$) on the $\text{Sqrt}(\text{SBR})$ response as determined by analysis of variance (ANOVA). In the second step, we identified the significant factors (via ANOVA) and estimated their coefficients. The nonsignificant factors that are not implicated in significant interactions were discarded in the final model. As shown in Figure 4C, the remaining factors were sorted by decreasing t ratio (i.e., the ratio of the coefficient estimate to its standard error), with the most substantial effects at the top. Not surprisingly, the factors *con* and *con* \times *vol* have significant positive coefficient estimates;

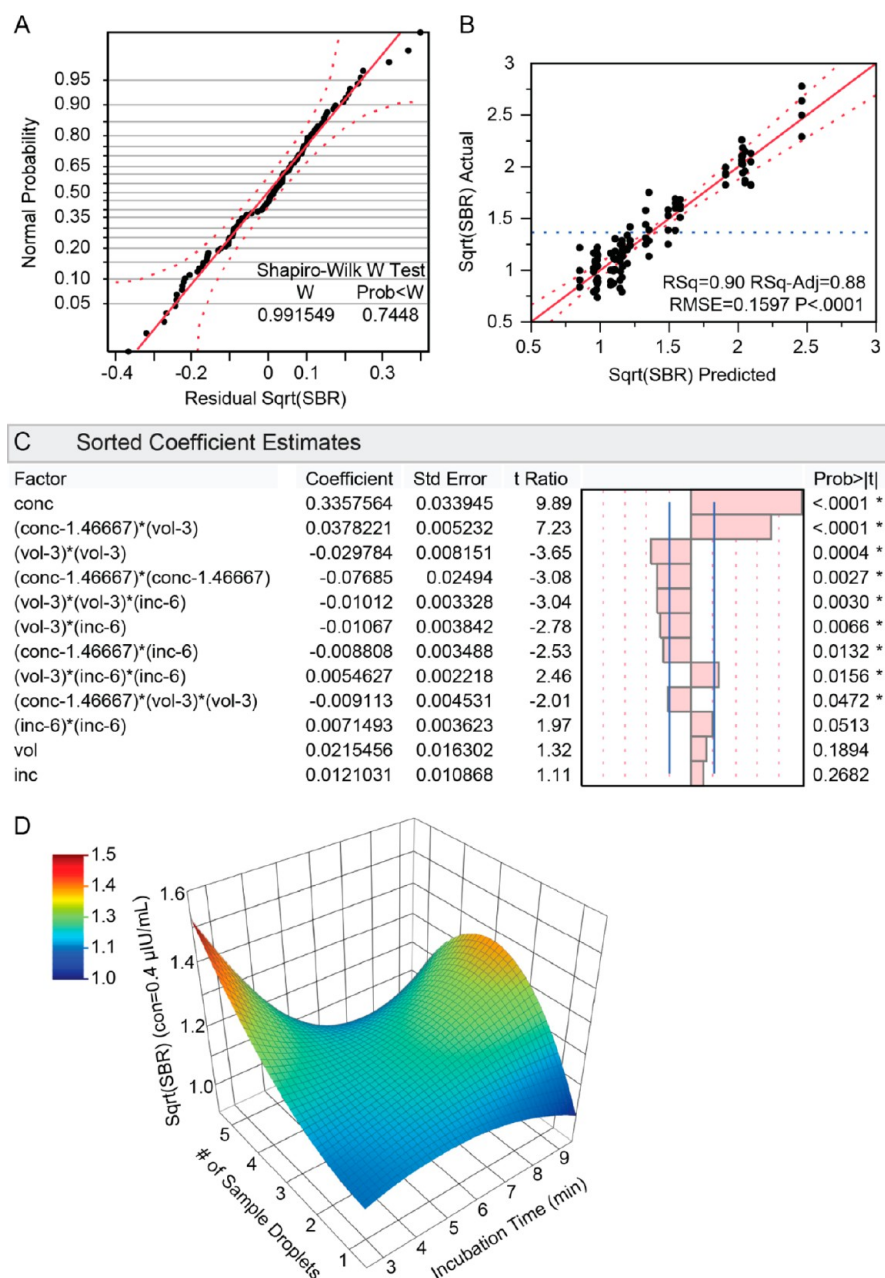


Figure 4. Design of experiments (DOE) analysis for TSH magnetic particle immunoassays. (A) Normal probability plot of the residuals and *W* test suggesting that the residuals are normally distributed. (B) Actual versus predicted plot superimposed with confidence curves (0.05). The plot correlates model predictions to actual data; the *p* value, R^2 , adjusted R^2 , and root mean square error (RMSE) for the correlation are indicated below the plot. (C) Coefficient estimates for centered polynomial regression sorted by decreasing *t* ratio; the bar graph plots the *t* ratios, and the vertical lines define the 0.05 significance level. (D) A three-dimensional surface corresponding to the square root of signal-to-background ratio response at 0.4 $\mu\text{IU/mL}$ TSH concentration showing the interaction between the sample incubation time and number of sample droplets (heat map with red = high response and blue = low response).

increasing TSH in the assay results in higher $\text{Sqrt}(\text{SBR})$. However, this increase eventually plateaus at higher *con* or *vol* as predicted by the negative coefficient quadratic factors (*con* \times *con* and *vol* \times *vol*). Interestingly, several interaction factors involving the sample incubation time (*vol* \times *vol* \times *inc*, *vol* \times *inc*, and *con* \times *inc*) have negative coefficient estimates, suggesting that a longer sample incubation time coupled with a high amount of TSH reduces the $\text{Sqrt}(\text{SBR})$. In the final step, the completed model, constructed from factors and coefficients in Figure 4C, was used to predict the optimal sample volume and sample incubation time for TSH immunoassays. The maximum

response was achieved at 4 $\mu\text{IU/mL}$ TSH concentration using five droplets of sample and a 3 min sample incubation time. These parameters were found to produce an optimal response at lower TSH concentrations, which is crucial for assay sensitivity. For example, at 0.4 $\mu\text{IU/mL}$ TSH concentration, the response surface increases for a higher sample volume and a lower sample incubation time, achieving the maximum response at five droplets and a 3 min sample incubation (Figure 4D).

Interestingly, these DOE data suggest that the new integrated platform allows for faster analyte binding to magnetic particles

relative to the initial prototype setup.²² This improvement is likely related to the rapid, continuous droplet mixing during sample incubation for the new setup; such uniform mixing was impossible to achieve using hand-held voltage probes in the prototype setup.²² A detailed comparison of the new integrated platform and the prototype setup is included in Table S1 in the Supporting Information.

Optimized Immunoassay. Using the results of the DOE analysis, we developed an optimized immunoassay protocol with improved performance relative to that from previous work.²² In pilot immunoassays, we observed high variability between replicates, with CVs ranging from 7% to 40%. This variability was caused by a flaw in the measurement procedure, in which samples assayed in parallel experience different wait times prior to measurement. Since there is a single, stationary PMT, droplets containing completed particle immunoassays must queue for analysis until the detection area becomes vacant. As a result, in the pilot immunoassays, the particles that are second in the queue must wait an extra 2 min in the wash buffer relative to the first set of particles (and so on). Interestingly, this extended wash buffer incubation caused a drop in the chemiluminescent signal of up to 45%. To circumvent this problem, we developed a new measurement procedure, in which wash buffer is immediately removed after the final wash step. Subsequently, the particles are resuspended in luminol–H₂O₂ substrate and mixed for 4 min. After mixing, the chemiluminescent signal becomes saturated, creating a stable measurement window (~1 min) for all particles to be analyzed sequentially. Using this new measurement procedure and the optimized parameters from DOE analysis (five pooled sample droplets and 3 min of sample incubation), immunoassays were implemented for various concentrations of TSH (0, 0.4, and 4 μ IU/mL) on the integrated platform. As shown in Table 1, the integrated platform exhibited better performance

Table 1. Comparison of TSH Immunoassay Performance

	prototype setup ²²	integrated platform
coefficient of variability (%)	9–21	6–10
limit of detection (absolute) (nIU)	2.0	0.6
limit of detection (concentration) (μ IU/mL)	0.83	0.15
sample volume (μ L)	2.4	4.0
sample incubation time (min)	6	3

when compared to the prototype setup in previous work.²² The reproducibility of the integrated platform is substantially better, with CVs ranging from 6% to 10%, and the integrated platform had a 3-fold or 5-fold lower LOD when calculated in terms of absolute amount or concentration, respectively. This improvement in the LOD (to 0.15 μ IU/mL) is critical, as it provides the capability to screen for hyperthyroidism ([TSH] < 0.3 μ IU/mL).³⁰ Finally, the sample incubation time was reduced by 2-fold because of the enhanced mixing offered by the integrated platform.

CONCLUSION

We developed an automated digital microfluidic platform for magnetic-particle-based immunoassays. This platform features a 90 Pogo pin interface for digital microfluidic control, an integrated detector for chemiluminescent detection, and a new magnet assembly that facilitates up to eight simultaneous digital

microfluidic magnetic separations. Most importantly, the new platform allows for the implementation of DOE optimization of immunoassay performance. As a test case, a three-level full factorial DOE analysis enabled the development of an optimized protocol that reduced the detection limit and sample incubation time by up to 5-fold and 2-fold, respectively. We propose that this new platform has great potential for the quantitative analysis of disease biomarkers at various near-patient settings worldwide.

ASSOCIATED CONTENT

Supporting Information

CAD rendering of the DMF device holder, illustration of the magnet assembly position, a detailed procedure for the characterization of the integrated PMT, calibration curves for HRP as detected by the integrated PMT and well-plate reader, simulations of the horizontal force component on the particle pellet, and a complete comparison of the prototype setup (from previous work) and the new integrated platform (in this work). This material is available free of charge via the Internet at <http://pubs.acs.org>.

AUTHOR INFORMATION

Corresponding Author

*E-mail: aaron.wheeler@utoronto.ca. Phone: (416) 946-3864. Fax: (416) 946-3865.

Author Contributions

^VK.C. and A.H.C.N. contributed equally to this work.

Notes

The authors declare no competing financial interest.

ACKNOWLEDGMENTS

We thank the Natural Sciences and Engineering Research Council of Canada (NSERC) and Abbott Diagnostics for financial support and CMC Microsystems for access to COMSOL Multiphysics. A.H.C.N. and R.F. thank the NSERC for graduate fellowships, and A.R.W. thanks the Canada Research Chair (CRC) Program for a CRC.

REFERENCES

- (1) Lequin, R. M. *Clin. Chem.* **2005**, *51*, 2415–2418.
- (2) Joyce, A. P.; Leung, S. S. *J. Immunol. Methods* **2013**, *392*, 12–23.
- (3) Mullin, R. *Chem. Eng. News* **2013**, *91*, 25–28.
- (4) Altekar, M.; Homon, C. A.; Kashem, M. A.; Mason, S. W.; Nelson, R. M.; Patnaude, L. A.; Yingling, J.; Taylor, P. B. *Clin. Lab. Med.* **2007**, *27*, 139–154.
- (5) Kalorama Information. The World Market for Point of Care (POC) Diagnostics, 2012.
- (6) Giljohann, D. A.; Mirkin, C. A. *Nature* **2009**, *462*, 461–464.
- (7) Ligler, F. S. *Anal. Chem.* **2008**, *81*, 519–526.
- (8) Whitesides, G. M. *Nature* **2006**, *442*, 368–373.
- (9) Ng, A. H. C.; Uddayasankar, U.; Wheeler, A. R. *Anal. Bioanal. Chem.* **2010**, *397*, 991–1007.
- (10) Chin, C. D.; Linder, V.; Sia, S. K. *Lab Chip* **2012**, *12*, 2118–2134.
- (11) Raamanathan, A.; Simmons, G. W.; Christodoulides, N.; Floriano, P. N.; Furmaga, W. B.; Redding, S. W.; Lu, K. H.; Bast, R. C., Jr.; McDevitt, J. T. *Cancer Prev. Res.* **2012**, *5*, 706–716.
- (12) Tarn, M. D.; Pamme, N. *Expert Rev. Mol. Diagn.* **2011**, *11*, 711–720.
- (13) Tekin, H. C.; Cornaglia, M.; Gijs, M. A. M. *Lab Chip* **2013**, *13*, 1053–1059.
- (14) Choi, K.; Ng, A. H. C.; Fobel, R.; Wheeler, A. R. *Annu. Rev. Anal. Chem.* **2012**, *5*, 413–440.

- (15) Jebrail, M. J.; Bartsch, M. S.; Patel, K. D. *Lab Chip* **2012**, *12*, 2452–2463.
- (16) Pollack, M. G.; Pamula, V. K.; Srinivasan, V.; Eckhardt, A. E. *Expert Rev. Mol. Diagn.* **2011**, *11*, 393–407.
- (17) Cho, S. K.; Moon, H.; Kim, C.-J. *J. Microelectromech. Syst.* **2003**, *12*, 70–80.
- (18) Sista, R. S.; Eckhardt, A. E.; Srinivasan, V.; Pollack, M. G.; Palanki, S.; Pamula, V. K. *Lab Chip* **2008**, *8*, 2188–2196.
- (19) Sista, R.; Hua, Z.; Thwar, P.; Sudarsan, A.; Srinivasan, V.; Eckhardt, A.; Pollack, M.; Pamula, V. *Lab Chip* **2008**, *8*, 2091–2104.
- (20) Vergauwe, N.; Witters, D.; Ceysens, F.; Vermeir, S.; Verbruggen, B.; Puers, R.; Lammertyn, J. *J. Micromech. Microeng.* **2011**, *21*, 054026.
- (21) Emani, S.; Sista, R.; Loyola, H.; Trenor, C. C. I.; Pamula, V. K.; Emani, S. M. *Blood Coagulation Fibrinolysis* **2012**, *23*, 760–768.
- (22) Ng, A. H. C.; Choi, K.; Luoma, R. P.; Robinson, J. M.; Wheeler, A. R. *Anal. Chem.* **2012**, *84*, 8805–8812.
- (23) Fobel, R.; Fobel, C.; Wheeler, A. R. *Appl. Phys. Lett.* **2013**, *102*, 193513.
- (24) Gassner, A.-L.; Abonnenc, M.; Chen, H.-X.; Morandini, J.; Jossierand, J.; Rossier, J. S.; Busnel, J.-M.; Girault, H. H. *Lab Chip* **2009**, *9*, 2356–2363.
- (25) Shah, G. J.; Chang-Jin, K. *J. Microelectromech. Syst.* **2009**, *18*, 363–375.
- (26) Neter, J.; Wasserman, W.; Kutner, M. H. *Applied Linear Statistical Models: Regression, Analysis of Variance, and Experimental Designs*, 3rd ed.; Richard D. Irwin, Inc.: Boston, MA, 1990.
- (27) Shih, S. C. C.; Barbulovic-Nad, I.; Yang, X.; Fobel, R.; Wheeler, A. R. *Biosens. Bioelectron.* **2013**, *42*, 314–320.
- (28) Kim, H.; Bartsch, M. S.; Renzi, R. F.; He, J.; Van de Vreugde, J. L.; Claudnic, M. R.; Patel, K. D. *J. Lab. Autom.* **2011**, *16*, 405–414.
- (29) Miller, E. M.; Wheeler, A. R. *Anal. Chem.* **2008**, *80*, 1614–1619.
- (30) Biondi, B.; Cooper, D. S. *Endocr. Rev.* **2008**, *29*, 76–131.
- (31) Audet, J. *Biotechnol. Bioeng.* **2010**, *106*, 173–182.
- (32) Teste, B.; Vial, J.; Descroix, S.; Georgelin, T.; Siaugue, J.-M.; Petr, J.; Varenne, A.; Hennion, M.-C. *Talanta* **2010**, *81*, 1703–1710.
- (33) Wang, W.; Horner, D. N.; Chen, W. L. K.; Zandstra, P. W.; Audet, J. *Biotechnol. Bioeng.* **2008**, *99*, 1261–1272.
- (34) Anderson, M. J.; Whitcomb, P. J. *RSM Simplified: Optimizing Processes Using Response Surface Methods for Design of Experiments*; Productivity Press: New York, 2004.
- (35) Montgomery, D. C. *Design and Analysis of Experiments*, 7th ed.; Wiley: Hoboken, NJ, 2008.